Does Uranus' asymmetric magnetic field produce a relatively weak proton radiation belt?

A. Masters[1], I. Charalambos[1], N. Rayns[1].

[1]Blackett Laboratory, Imperial College London, Prince Consort Road, London, SW7 2AZ, UK.

Key points:

1. Asymmetry in Uranus' magnetic field perturbs motion of radiation belt particles with respect to their motion in a planet-centered dipole.
2. This perturbation is more significant the greater the gyroradius of the particle, making the highest energy ions the most affected.
3. Degraded trapping of these particles compared to a planet-centered dipole may explain the weak proton radiation belt observed by *Voyager 2*.

This article has been accepted for publication and undergone full peer review but has not been through the copyediting, typesetting, pagination and proofreading process, which may lead to differences between this version and the Version of Record. Please cite this article as doi: 10.1029/2022GL100921.

Abstract

Since the *Voyager 2* flyby in 1986 the radiation belts of Uranus have presented a problem for physicists. The observations indicate the electron radiation belt is far more intense than the proton radiation belt, and while the electron intensities are close to the upper theoretical limit, proton intensities are well below. Here we propose the relatively weak proton radiation belt could be due to Uranus' asymmetric magnetic field. We model test particle motion through the field to show that perturbations arising from asymmetry are greater the larger the particle gyroradius, predominantly affecting $\gtrsim$100-keV protons. For these particles, more rapid changes in maximum distance from the planet during a bounce motion promote trajectory evolution into regions where they could be lost through impact with the rings, impact with the atmosphere, or to the distant magnetosphere and solar wind. We suggest this could explain a relatively weak proton radiation belt at Uranus.

Keywords: Uranus, radiation belts, planetary magnetic field, finite-gyroradius effects.

1. Introduction

The *Voyager 2* spacecraft flew by Uranus in 1986, the only encounter with our nearest ice giant planet to date [*Stone & Miner*, 1986]. The data returned provide us with a "snapshot" of the planetary system that has allowed leaps forward in our understanding, but ultimately has also produced a long list of fundamental open questions that have since driven calls for further exploration [e.g., *Fletcher et al*., 2020]. At the time of writing a flagship mission to Uranus has been prioritized, and magnetospheric science is one of the pillars upon which this project will be built (see the review by *Kollmann et al*. [2020]). Understanding the radiation environment of energetic charged particles is one of the major themes within this field, and a mystery concerning Uranus' radiation belts has persisted since the 1980s.

Radiation belts form in the highly tenuous space plasma around a magnetized planet, like the Earth (see the review by *Li & Hudson* [2019]). Energetic charged particles become trapped by the planetary magnetic field structure, typically within ~10 planetary radii [*Mauk & Fox*, 2010; *Mauk*, 2014]. The particles gyrate around the magnetic field direction while also moving along it, undergoing magnetic mirroring as they approach the planet in either hemisphere where the field strength increases, and drifting around the planet on a longer timescale due to field gradient and curvature. At most magnetized planets the field structure in which these particles move is well-approximated by a dipole centered on the planet (see the review by *Schubert & Soderlund* [2011]), and so the latter drift is effectively azimuthal with respect to the dipole axis. Particles are differentiated by species (electron or ion), energy, and approximate magnetic dipole "L-shell" on which they move. These shells are surfaces defined by all the dipole field lines that cross the dipole equator at the same radial distance from the planet's center, given this distance as an identifier.

Field and particle instruments on the *Voyager 2* spacecraft allowed *in situ* measurements during the 1986 flyby that confirmed Uranus' magnetic field and the presence of both electron and proton radiation belts [*Ness et al*., 1986; *Cheng et al*., 1987; *Connerney et al*., 1987; *Mauk et al*., 1987]. Observations were made as close as ~4.2 planetary radii (R_U, 1 R_U = 25,559 km), detecting particle energies up to order MeV. At 1 MeV and at the same location, the electron radiation belt intensity was higher than that of the proton radiation belt by a factor of ~100. Intense whistler mode hiss and chorus waves were also identified [*Coroniti et al*., 1987], as was evidence for sculpting of the radiation belts by Uranus' five large moons [*Hood*, 1989; *Selesnick & Stone*, 1991].

Comparison with theory sheds further light on the observed state of Uranus' radiation belts. The Kennel-Petschek (K-P) limit is a predicted upper bound on integral particle intensities above a specified energy that reflects the strong suppression of these intensities that can result from wave-particle interactions, where the waves in question are whistler waves for electrons and electromagnetic ion cyclotron waves for protons [*Kennel & Petschek*, 1966]. Updated application to Uranus has shown that the more intense electron radiation belt is close to this limit at energies up to ~1 MeV [*Mauk & Fox*, 2010], whereas the less intense proton radiation belt is well below it at all energies [*Mauk*, 2014]. For context, the intensities of both the electron and proton radiation belts of Earth and Jupiter challenge their respective K-P limits over certain energy ranges [*Mauk & Fox*, 2010; *Mauk*, 2014].

This all leads to two key open questions concerning Uranus' radiation belts (see the review by *Kollmann et al*. [2020]). Firstly, why is the electron radiation belt so intense despite the absence of a strong source population of lower energy electrons and the presence of strong plasma wave activity that acts to destroy it [*Coroniti et al*., 1987; *McNutt et al*., 1987; *Mauk et al*., 1994]? Secondly, in contrast, why is the proton radiation belt intensity so weak? Here we propose an answer to the second question.

2. Modeling the motion of test protons in Uranus' asymmetric magnetic field

We hypothesize that Uranus' proton radiation belt is weak because of asymmetry in Uranus' magnetic field with respect to a planet-centered dipole, which is more significant than at the magnetized planets closer to the Sun (see the review by *Schubert & Soderlund* [2011]). We expect this degrades the ability of the field to trap the energetic protons that have the largest radii of gyromotion ("gyroradii"), compared to a planet-centered dipole. To test this hypothesis, we perform simple numerical modeling that predicts how proton "test particles" move through the three-dimensional planetary magnetic field structure. In each simulation we specify the initial state of a test proton and then calculate a numerical solution to its equation of motion. This approach neglects inter-particle interactions, how the test particle may influence the field itself, and wave-particle interactions, among other physics. Nonetheless, test particle simulations are a powerful diagnostic tool.

Voyager 2 observations showed that on large scales Uranus' magnetic field structure can be approximated as a dipole with an axis tilted with respect to Uranus' rotation axis, and a center offset with respect to Uranus' center [*Ness et al*., 1986]. However, in the vicinity of the radiation belts a more accurate spherical harmonic model of the field is required [*Connerney et al*., 1987], and such models are defined in a coordinate system that has its origin coincident with Uranus' center. Here we use the spherical harmonic model reported by *Herbert* [2009], which is based on a combination of *Voyager 2* magnetic field observations and remote sensing of Uranus' auroral emissions.

The lowest-degree component of a spherical harmonic model is the dipole, followed by the quadrupole, and then octupole. The addition of best-fit components represents a model of the field [e.g., *Connerney*, 1993]. For Uranus, largest uncertainties in the dipole, quadrupole, and octupole Gauss coefficients are of order 1%, 10%, and 100%, respectively [*Connerney et al*., 1987; *Herbert*, 2009]. Furthermore, the dipole and quadrupole moments are comparable, whereas the octupole component is ~50% smaller. In this work we therefore take Uranus' field as the sum of best-fit dipole and quadrupole components [*Herbert*, 2009]. Note that only using the dipole gives a planet-centered field structure with symmetry comparable to magnetized planets closer to the Sun, which is unrealistic. Adding the quadrupole to the dipole introduces asymmetry that is more realistic, producing a structure that tends to the "offset-tilted dipole" approximation when viewed on larger scales.

Our base coordinate system is that in which the spherical harmonic field structure is defined. This has its origin at Uranus' center, *z*-axis aligned with Uranus' rotation axis, and the system rotates with the planet. The *x*-axis and *y*-axis complete the right-handed Cartesian set. From this system we define our model system by performing rotations about the *x*-axis and *y*-axis in sequence to produce a *z*-axis aligned with Uranus' dipole axis. As outlined above, the dipole defining our coordinate system is unlike Uranus' true field structure. A rationale for use of this system is that particle motion in planet-centered dipoles is well-understood theoretically, and addition of Uranus' quadrupole introduces asymmetry. This makes comparison between dipole and dipole-plus-quadrupole field structures in our chosen system well-suited to identifying associated perturbations of particle motion.

We present vector components in spherical polar coordinates based on this system, where r is range, θ is co-latitude, and ϕ is azimuth. We do not treat rotation of the field structure over a Uranus rotation period of 17.24 hours [*Desch et al*., 1986], a timescale that is considerably longer than the bounce times of radiation belt particles. The equation of motion for a test proton moving through Uranus' magnetic field is

$$\gamma m_0 \frac{d\underline{v}}{dt} = q\underline{v} \times \underline{B} \qquad (1),$$

where γ is the relativistic factor, defined as

$$\gamma = \frac{1}{\sqrt{1-\frac{v^2}{c^2}}} \qquad (2),$$

m_0 is the proton rest mass, $\underline{v}$ is the proton velocity, t is time, q is the charge of the proton, and $\underline{B}$ is the magnetic field vector at the particle's position. If we calculate a numerical solution to Equation 1 over a given time step then the position vector of the particle, $\underline{r}$, can be updated using

$$\underline{v} = \frac{d\underline{r}}{dt} \qquad (3).$$

To explore the impact of asymmetry in Uranus' magnetic field on radiation belt proton trajectories we model the mirroring of particles at both $z > 0$ and at $z < 0$. We refer to the region $z > 0$ as the "northern hemisphere" and $z < 0$ as the southern hemisphere, defined with respect to Uranus' dipole. We identified a forward-difference sixth-order Runge-Kutta method as appropriate to solve Equation 1, given its accuracy predicting the motion of test protons in Earth dipolar field over multiple bounce motions [e.g., *Soni et al*., 2020]. We use an adaptive time step, set as the gyroperiod of the particle at the last point in time divided by 50. For more details of the numerical scheme we refer the reader to *Luther* [1968], *Soni et al*. [2020], and the publicly available code.

3. Results

Figure 1 shows the modeled motion of a 30-keV test proton through both Uranus' dipole and dipole-plus-quadrupole field structures. Figure 2 shows the modeled motion of a 3-MeV test proton, also through both a dipole and dipole-plus-quadrupole structure. As discussed in Section 2, note that dipole simulations are for reference, dipole-plus-quadrupole simulations are more realistic. These energies represent the approximate limits of the radiation belt proton energy spectrum measured by *Voyager 2* [e.g., *Mauk*, 2014].

Different energies aside, all other initial conditions are common to the four example simulations. We set the initial position of the instantaneous center of particle gyromotion (the "guiding center") at a range of 6.5 R_U on the dipole equator (the *x*-*y* plane) and on the positive *x*-axis (ϕ = 0°). The magnetic field strength at the guiding center defines the initial gyrofrequency and gyroradius of the test proton, and its initial position vector was set to be one gyroradius away from the guiding center perpendicular to the field and at the closest point to the planet over a full circular gyromotion (initial "gyrophase"). The initial velocity of the test proton made an angle of 175° to the local magnetic field direction (the "pitch angle", α), meaning it was initially moving northward. All simulations were run until a full bounce motion had taken place; i.e., until the test particle next crossed the dipole equator moving northward. Full bounce motion of a 30-keV test proton takes ~5 minutes whereas full bounce motion of a 3-MeV test proton takes ~30 seconds, with little sensitivity to the prescribed field structure.

Focusing first on the dipole-field reference cases, based on conservation of the first adiabatic invariant of the particles we expect the mirror points of both the 30-keV and 3-MeV test protons to be at a range of ~1.56 R_U and with a smallest angle to the *z*-axis of ~29.3°. This applies to mirroring in both hemispheres, a consequence of the rotational symmetry of the dipole about the *z*-axis. For the 30-keV test proton the ranges are 1.56 R_U and angles are 29.4° in both hemispheres, whereas for the 3-MeV test proton the ranges are 1.76 R_U and the angles are 31.3°. In the former case, deviation from theory places a bound on the numerical error in our modeling results, and in the latter case it indicates sensitivity to initial gyrophase (i.e., finite-gyroradius effects not accounted for in the predictions). The magnetic field gradient-curvature drift of a test proton, $\underline{v_d}$, assuming that no electrical currents flow in the plasma, can are defined as

$$\underline{v_d} = \frac{\gamma m_0}{2qB}\left(v_\perp^2 + 2v_\parallel^2\right)\frac{\underline{B}\times\nabla B}{B^2} \qquad (4)$$

where $v_\perp$ is the component of the particle velocity that is perpendicular to the local magnetic field and $v_\parallel$ is the component of the particle velocity that is parallel to the local magnetic field. Calculation of this drift velocity for both the dipole-field cases indicates the purely azimuthal drift that is expected from the dipole's rotational symmetry, which is faster when the particle is near the dipole equator where its gyroradius is largest. The 3-MeV test proton undergoes much faster drift than the 30-keV test proton due to its typically larger gyroradius.

Focusing now on the more realistic dipole-plus-quadrupole field cases, there are some significant differences with the companion dipole-field reference cases. These arise from the asymmetry the addition of the quadrupole has introduced, and so we identify them as associated perturbations. The quadrupole component of the field becomes stronger relative to the dipole component the closer to the planet, significantly affecting trajectories of both the 30-keV and 3-MeV test protons near their mirror points. The field is weaker in the North than the South, often illustrated using the offset dipole approximation, meaning both protons mirror at lower altitudes in the North. The gradient-curvature drift of the test protons is no longer purely azimuthal, with non-zero r-components and non-zero θ-components. Compared to the north-south asymmetry in mirror point altitudes and resulting "atmospheric loss cones" that do not depend on particle energy, the perturbation of gradient-curvature drifts is more relevant in the context of our hypothesis because it is sensitive to this energy.

Figure 3 explores this effect with further example simulations using the dipole-plus-quadrupole field. Initial conditions are as in Figures 1 and 2, with the following differences. A range of proton energies between the two extremes are now treated, and eight initial gyrophases that are in equally spaced increments of 45° are considered. At each energy, a set of eight particles (differentiated by gyrophase) were sent to mirror in the North (initial pitch angles of 175°) and a set of eight were sent to mirror in the South (initial pitch angles of 5°). We consider these "mirroring events" separately because of the north-south asymmetry in the field.

As a proxy for particle trajectory evolution, we subtract initial maxima in guiding center radial distance from the maxima after mirroring, giving a value of Δr_{max}, which we divide by time taken to move from one point to the other, t_m, to give a value of $\Delta r_{max}/t_m$. This describes how the bounce motion of the particle evolves with time, with positive values indicating "expanding" trajectories that extend to farther radial distances with each mirror event and negative values indicating "contracting" trajectories becoming confined closer to the planet with each event. Initial guiding center positions on the dipole equator are not maxima in radial distance of each particle's guiding center during a bounce motion, so we run each simulation backwards in time until we have ensured we capture this distance. We then run each simulation forwards in time until the particle passes the next maxima in radial distance.

In the region chosen for these examples, mirroring in the North favors positive $\Delta r_{max}/t_m$, whereas mirroring in the South exclusively favors negative $\Delta r_{max}/t_m$. In both hemispheres the magnitude and spread of values with gyrophase increase with test proton energy, consistent with a finite-gyroradius effect. This is non-linear, with rates becoming more significant above ~100 keV and having the most impact on particles above ~1 MeV. The range of values for dipole-field simulations is indicated by gray shading for reference, confirming that asymmetry in Uranus' field is responsible. For a 30-keV proton the value of $\Delta r_{max}/t_m$ is of order 10^{-5} R_U s^{-1}, and so over half a bounce motion the change in r_{max} is ~ 0.002 R_U. In contrast, for a 3-MeV proton the value of $\Delta r_{max}/t_m$ is of order 10^{-3} R_U s^{-1}, and so over half a bounce motion the change in r_{max} is ~0.02 R_U. A 3-MeV proton bounces ~10 times in the time it takes a 30-keV proton to bounce once for our example initial conditions.

Figure 4 extends our treatment to the global field structure, now considering different ranges and azimuths of the initial guiding center position in the dipole equator (i.e., no longer just considering r = 6.5 R_U and ϕ = 0° as an example). We now only model 3-MeV test protons, and use initial pitch angles of 160° (mirroring in the North, *z* > 0) and 20° (mirroring in the South, *z* < 0) to ensure no particles precipitate into the atmosphere. In both panels the *xy* plane is shown as viewed from along the negative *z*-axis (i.e., looking down on the dipole magnetic equator from the North). The data points span the full range of initial azimuth and a range of initial radial distances from the planet from 3 to 10 R_U. Each data point corresponds to a set 3-MeV test proton mirroring event simulations, following the same approach as for the results presented in Figure 3. The color of a data point in Figure 4 indicates the mean value of $\Delta r_{max}/t_m$ over all initial gyrophases. For each point there is a scatter with gyrophase similar to those illustrated at 3 MeV in Figure 3. Green data points have a mean value within the range of values for a dipole-field simulation, and data points surrounded by a circle of the same color are those where the value of $\Delta r_{max}/t_m$ is exclusively positive or negative across all initial gyrophases.

Figure 4 shows that the mean values of $\Delta r_{max}/t_m$ for our example initial guiding center position are not a constant across this parameter space in either hemisphere. Unlike Figure 3 examples, a similar, but not identical pattern is present in both hemispheres, suggesting mirroring in both the North and the South over a full bounce motion reinforces the sense of trajectory evolution. Blue data points indicate regions where mirroring in a hemisphere causes the bounce trajectory of a test proton to contract, whereas red data points indicate where these trajectories are expanding. The prevailing effect is contraction in both hemispheres, spanning a similar, wide range of >180° in azimuth. There is also a more limited region of expansion that is similar in both hemispheres, starting closest to the planet over <90° in azimuth but not extending to the upper limit of initial radial distance.

4. Discussion

The modeling results presented in Section 3 support our assertion that the presence of asymmetry in Uranus' magnetic field degrades the ability of the structure to trap particles, compared to a planet-centered dipole that is a more representative of planetary magnetic fields closer to the Sun (see the review by *Schubert & Soderlund* [2011]). We have highlighted a specific aspect of this concerning drift motions, which affects different particle species and energies to different extents. Azimuthal gradient-curvature drift of particles in a dipole is optimal for confinement, and so deviation away from this magnetic structure will perturb these drift motions and tend to promote particle loss from the system. This loss can result from impact with the planet itself, or the planetary rings, or loss to the distant magnetosphere, depending on whether particle trajectories close to the planet contract or far from the planet expand, respectively. Particles with the largest gyroradii undergo the fastest drift, making this trapping degradation most significant for ions at the highest energies.

We therefore suggest these results are consistent with our hypothesis that Uranus' weak proton radiation belt could be due to the asymmetric planetary magnetic field. Preferential loss of energetic protons may explain the low intensity of >100-keV protons in the radiation belt compared to the K-P limit [Mauk, 2014], which does not account for this effect. Note that electron gyroradii are ~40 times smaller than proton gyroradii at a given energy, and so even at the largest electron energies of ~3 MeV the gyroradius of these particles will be far below the gyroradius of a 30-keV proton. This makes the effect on electrons weaker than all the test protons we have considered. Inclusion of even higher-degree structure of Uranus' magnetic field would likely strengthen our conclusion, but we suggest the contribution will be negligible because higher-degree moments are already constrained to be lower than that of the quadrupole, and the strength of these field components decays more rapidly with distance from the planet [*Connerney*, 1993; *Herbert*, 2009].

Our conclusion is tentative, with further work required to more firmly establish if our hypothesis is correct. It remains to be seen if the effect quantitatively translates into predicted radiation belt proton intensities that match those measured by *Voyager 2*. Referring to Figure 4, while there appears to be a net contraction of energetic proton trajectories towards Uranus over time, this should be treated with caution as these results do not treat multiple bounce motions. Loss of particles at both the inner and outer limits of radial distance is a robust expectation underpinning our proposition, but scatter with gyrophase in particular makes the long-term evolution of individual proton trajectories unclear. Further work is needed to address this, involving both significant extension of test particle modeling to cover longer timescales with the Boris algorithm and more sophisticated numerical modeling that captures additional physics such as wave-particle interactions. The present study clearly has no impact on explaining why Uranus' electron radiation belt is so strong (see the review by *Kollmann et al*. [2020]). Ultimately, further *in situ* measurements will be essential for progress on this topic.

Acknowledgements

AM is supported by a Royal Society University Research Fellowship.

Open Research

Computer code and derived data shown in Figures 1–4 are publicly available in the Zenodo data repository (https://doi.org/10.5281/zenodo.7348000).

Reference list

Cheng, A. F., et al. (1987), Energetic ion and electron phase space densities in the magnetosphere of Uranus, *J. Geophys. Res.*, *92*, 15315-15329, doi:10.1029/JA092iA13p15315.

Connerney, J. E. P., et al. (1987), The magnetic field of Uranus, *J. Geophys. Res.*, *92*, 15329-15336, doi:10.1029/JA092iA13p15329.

Connerney, J. E. P. (1993), Magnetic fields of the outer planets, *J. Geophys. Res.*, *98*, 18659-18680, doi:10.1029/93JE00980.

Coroniti, F. V., et al. (1987), Whistler mode emissions in the Uranian radiation belts, *J. Geophys. Res.*, *92*, 15234-15248, doi:10.1029/JA092iA13p15234.

Desch, M. D., et al. (1986), The rotation period of Uranus, *Nature*, *322*, 42-43, doi:10.1038/322042a0.

Fletcher, L. N., et al. (2020), Ice giant system exploration in the 2020s: an introduction, *Phil. Trans. R. Soc.*, *378*, article id.20190473, doi:10.1098/rsta.2019.0473.

Herbert, F. (2009), Aurora and magnetic field of Uranus, *J. Geophys. Res.*, *114*, doi:10.1029/2009JA014394.

Hood, L. L. (1989), Radial diffusion in the Uranian radiation belts: inferences from satellite absorption loss models, *J. Geophys. Res.*, *94*, 15077-15088, doi:10.1029/JA094iA11p15077.

Kennel, C. F., and H. E. Petschek (1966), Limit on stably trapped particle fluxes, *J. Geophys. Res.*, *71*, 1-28, doi:10.1029/JZ071i001p00001.

Kollmann, P., et al. (2020), Magnetospheric Studies: A Requirement for Addressing Interdisciplinary Mysteries in the Ice Giant Systems, *Space Sci. Rev.*, *216*, 78, doi:10.1007/s11214-020-00696-5.

Li, W., and M. K. Hudson (2019), Earth's Van Allen Radiation Belts: From Discovery to the Van Allen Probes Era, *J. Geophys. Res.*, *124*, 8319-8351, doi:10.1029/2018JA025940.

Luther, H. (1968), An explicit sixth-order Runge-Kutta formula, *Math. Comput.*, 22, 434-436, doi:10.1090/S0025-5718-68-99876-1.

Mauk, B. H., et al. (1987), The hot plasma and radiation environment of the Uranian magnetosphere, *J. Geophys. Res.*, *92*, 15283-15308, doi:10.1029/JA092iA13p15283.

Mauk, B. H., Keath, E. P., and S. M. Krimigis (1994), Unusual satellite-electron signature within the Uranian magnetosphere and its implications regarding whistler electron loss processes, *J. Geophys. Res.*, *99*, 19441-19450, doi:10.1029/94JA01658.

Mauk, B. H., and N. J. Fox (2010), Electron radiation belts of the solar system, *J. Geophys. Res.*, *115*, doi:10.1029/2010JA015660.

Mauk, B. H. (2014), Comparative investigation of the energetic ion spectra comprising the magnetospheric ring currents of the solar system, *J. Geophys. Res.*, *119*, doi:10.1002/2014JA020392.

McNutt, R. L., et al. (1987), Low-energy plasma observations in the magnetosphere of Uranus, *J. Geophys. Res.*, *92*, 4399-4410, doi:10.1029/JA092iA05p04399.

Ness, N. F., et al. (1986), Magnetic fields at Uranus, *Science*, *233*, 85-89, doi:10.1126/science.233.4759.85.

Schubert, G., and K. M. Soderlund (2011), Planetary magnetic fields: Observations and models, *Phys. Earth Planet. Inter.*, *187*, 92-108, doi:10.1016/j.pepi.2011.05.013.

Selesnick, R. S., and E. C. Stone (1991), Energetic electrons at Uranus: Bimodal diffusion in a satellite limited radiation belt, *J. Geophys. Res.*, *96*, 5651-5665, doi:10.1029/90JA02696.

Soni, P. K., et al. (2020), L-shell and energy dependence of magnetic mirror point of charged particles trapped in Earth's magnetosphere, *Earth Planets Space*, *72*, doi:10.1186/s40623-020-01264-5.

Stone, E. C., and E. D. Miner (1986), The Voyager 2 Encounter with the Uranian System, *Science*, *233*, 39-43, doi:10.1126/science.233.4759.39.

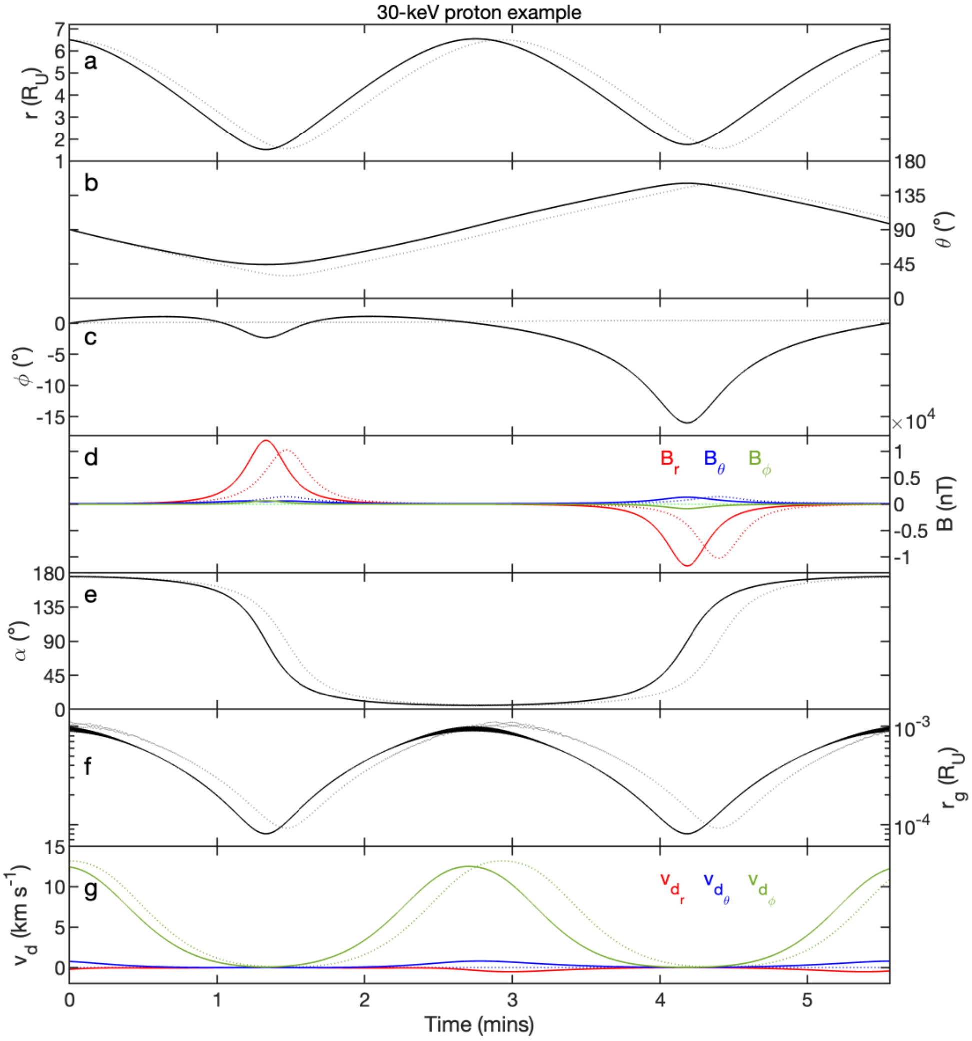

Figure 1. Modeled example trajectories of a 30-keV test proton in Uranus' dipole and dipole-plus-quadrupole magnetic fields over a full bounce motion. See Section 2 for a description of the coordinate system used. (a, b, c) Particle position vectors given in spherical polar coordinates, r, θ, and ϕ, respectively. (d) Magnetic field vectors at particle positions, given as the components of the field in the local r, θ, and ϕ directions (red, blue, and green, respectively). (e) Particle pitch angle, α. (f) Particle gyroradius, r_g. (g) Particle gradient-curvature drift velocities, $\underline{v_d}$, given as the components of the velocity in the local r, θ, and ϕ directions (red, blue, and green, respectively). In all panels the dashed lines correspond to dipole-only simulation results, whereas solid lines correspond to the dipole-plus-quadrupole simulation.

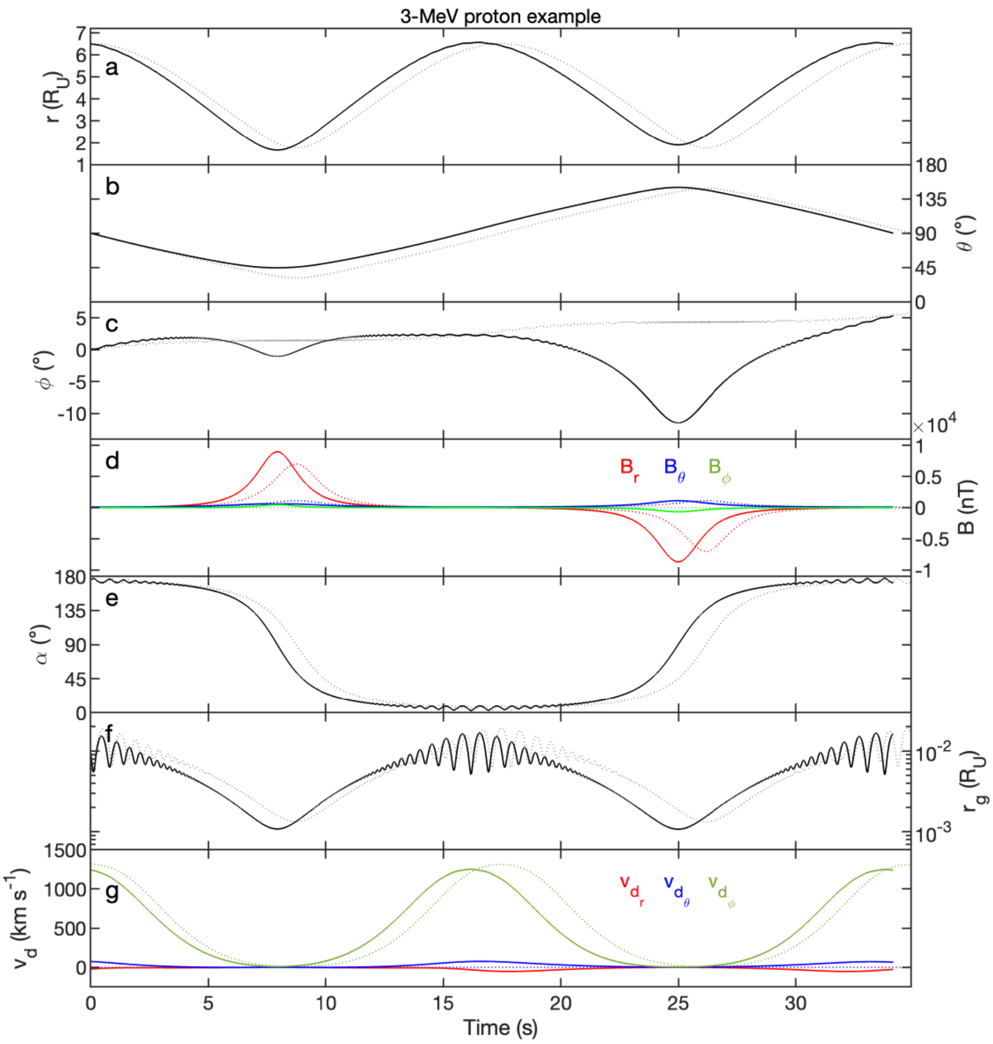

Figure 2. Modeled example trajectories of a 3-MeV test proton in Uranus' dipole and dipole-plus-quadrupole magnetic fields over a full bounce motion, using the same format as Figure 1.

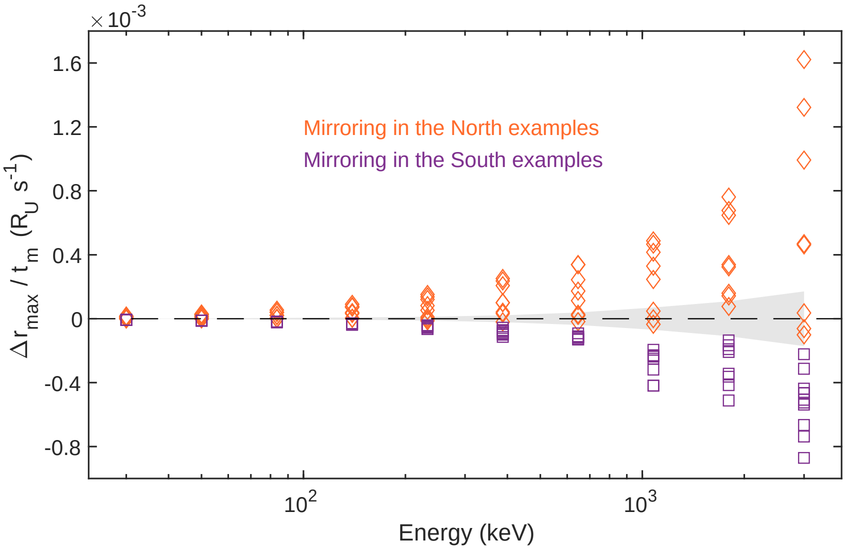

Figure 3. Calculated values of $\Delta r_{max}/t_m$ for modeled example test proton trajectories, covering a range of particle energies and initial gyrophases (see Section 3 for further details). Values corresponding to mirroring in the North are shown in orange and values corresponding to mirroring in the South are shown in purple. The gray-shaded region indicates the range of values for reference dipole simulations.

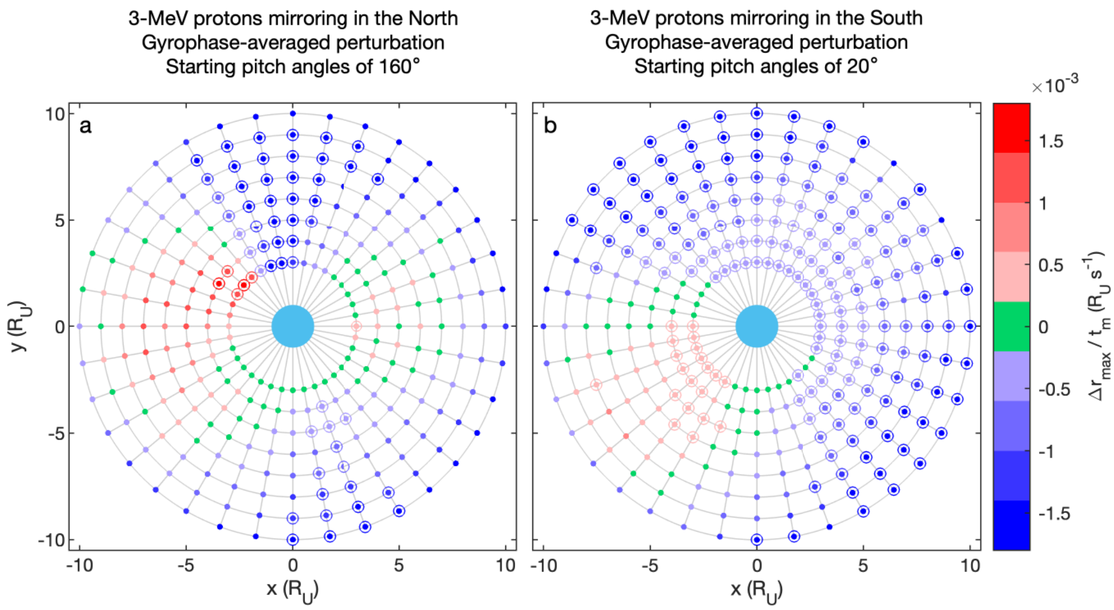

Figure 4. Modeled gyrophase-averaged values of $\Delta r_{max}/t_m$ for 3-MeV test protons across a range of initial guiding center positions (see Section 3 for further details). (a) Values for mirroring in the North (initial pitch angles of 160°). (b) Values for mirroring in the South (initial pitch angles of 20°). In both panels the dipole magnetic equator is shown as viewed from the North and Uranus is the pale-blue-filled circle at the origin.